SCIENTIFIC REPORTS

High-entropy alloy strengthened by *in situ* formation of entropy-stabilized nano-dispersoids

Bharat Gwalani[1], Rizaldy M. Pohan[2], Junho Lee[2], Bin Lee[3], Rajarshi Banerjee[1], Ho Jin Ryu[4] & Soon Hyung Hong[2]

A significant increase in compressive yield strength of the $Al_{0.3}CoCrFeMnNi$ high-entropy alloy (HEA) from 979 MPa to 1759 MPa was observed upon the introduction of 3 vol.% Y_2O_3. The HEAs were processed using spark plasma sintering of mechanically alloyed powders. Transmission electron microscopy and atom probe tomography confirmed the presence of compositionally complex nano-dispersoids in the Y_2O_3-added HEA. The significant increase in strength can be attributed to the nano-dispersoid strengthening coupled with grain refinement. Therefore, the *in-situ* formation of the compositionally complex nanoscale dispersoids during the alloy processing could be a novel approach to create entropy-stabilized oxide particles in strengthening of HEAs.

High-entropy alloys (HEAs) are a new class of metallic alloys, defined by Yeh *et al.*[1] as an alloy system consisting of five or more metallic elements with concentrations in the range of 5–35 at%. As their name suggests, HEAs exhibit a high configurational entropy, which favors the formation of a solid solution instead of intermetallic compounds. They attract significant research interests owing to their high strength, thermal stability, wear resistance, corrosion resistance, etc.

Amongst the myriad of HEA systems, CoCrFeMnNi is one of the most intensively investigated alloys owing to its attractive properties including cryogenic mechanical properties[2], thermodynamic stability[3], and malleability. Its microstructure consists of a single face-centered-cubic (*fcc*) solid solution, initially revealed by Cantor *et al.*[4].

Although it exhibits various desirable properties, the mechanical strength of CoCrFeMnNi is very low[5]. CoCrFeMnNi HEA is commonly synthesized using melting and casting processes. However, ingot metallurgy tends to create coarse grains with heterogeneous dendritic structures during cooling[6]. In order to improve its mechanical properties, additional thermomechanical methods have to be employed, such as rolling, high-pressure torsion[3], and swaging[7], after arc melting.

An alternative method to synthesize HEAs is powder metallurgy processing including mechanical alloying (MA) and spark plasma sintering (SPS). A target material, in the form of powder, is subjected to a repetitive cycle of cold welding, fracturing, and rewelding using high-energy ball milling to achieve solid-state alloying. The alloyed powders are then subjected to compaction and sintering. Using the powder metallurgy process, nano-grains can be obtained, which improve the mechanical properties of the HEA[8].

The addition of aluminum to CoCrFeMnNi can enhance its mechanical properties through the increase of the lattice distortion. He *et al.*[9] reported that the addition of Al not only decreased the density of the alloy but also increased the yield strength through solid solution strengthening and formation of a harder body-centered cubic (*bcc*) phase[10,11] with the further addition of aluminum.

Another strengthening method is oxide dispersion strengthening (ODS), based on oxides such as Al_2O_3, TiO_2, ZrO_2, and Y_2O_3, which restrict dislocation motion by dispersion strengthening and restrain grains' growth owing to the grain-pinning effect[12]. Owing to its high hardness (~1,020 Hv) and thermal stability[13], Y_2O_3 is commonly used as a dispersoid for ODS alloys. ODS effectively strengthened the CoCrFeMnNi HEA from 1 GPa

[1]Department of Materials Science and Engineering, University of North Texas, 1155 Union Circle, Denton, TX, 76203, USA. [2]Department of Materials Science and Engineering, Korea Advanced Institute of Science and Technology, 291 Daehak-ro, Yuseong-gu, Daejeon, 34141, Republic of Korea. [3]Korea Institute of Rare Metals, Gaetbeol-ro 12, Incheon, Republic of Korea. [4]Department of Nuclear and Quantum Engineering, Korea Advanced Institute of Science and Technology, 291 Daehak-ro, Yuseong-gu, Daejeon, 34141, Republic of Korea. Bharat Gwalani and Rizaldy M. Pohan contributed equally. Correspondence and requests for materials should be addressed to H.J.R. (email: hojinryu@kaist.ac.kr) or S.H.H. (email: shhong@kaist.ac.kr)
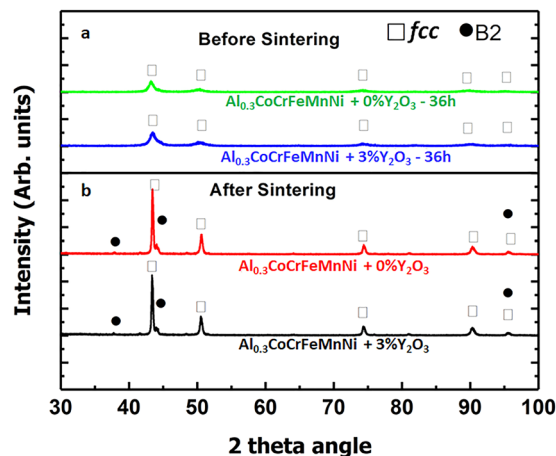
Figure 1. X-ray Diffraction: (**a**) XRD peaks of $Al_{0.3}CoCrFeMnNi$ without Y_2O_3 and with 3% at. Y_2O_3 after 36 hours of milling. (**b**) XRD peaks of sintered $Al_{0.3}CoCrFeMnNi$ without Y_2O_3 and with 3% at. Y_2O_3 after milling.

to 1.2 GPa at room temperature, and from 400 MPa to 800 MPa at 800 °C[14]. Even though Al-containing HEAs have been extensively investigated owing to the promising strength-ductility combinations[1,9,15], there are no reports on ODS of Al-containing CoCrFeMnNi HEAs. This study focuses on the effect of introducing Y_2O_3 in the $Al_{0.3}CoCrFeMnNi$ HEA, fabricated using MA and spark plasma sintering. The *in-situ* reaction of Y_2O_3 with the other substitutional elements (from the solid-solution HEA matrix) leads to a complex dispersoid. This is the first report that employs atom probe tomography (APT) to accurately measure the composition and morphology of the nanoscale oxide dispersoids.

Results and Discussion

XRD analyses during MA and after SPS.
Figure 1(a) shows the XRD results after the milling of the $Al_{0.3}CoCrFeMnNi$ powders. After 36 h of milling, only *fcc* peaks were observed for both samples, alloy powders without Y_2O_3 (0% Y_2O_3) and with 3% Y_2O_3. The milling conditions optimized for $Al_{0.3}CoCrFeMnNi$ high entropy alloys were used in this study. The details of the milling conditions and the microstructural evolution of the mechanically alloyed powder were described in our previous paper by the authors on $Al_{0.3}CoCrFeMnNi$[16]. Figure 1 shows that the diffraction peaks of $Al_{0.3}CoCrFeMnNi$ and ODS HEA are almost similar because the addition of Y_2O_3 did not change the milling process significantly The *fcc* peaks had a low intensity and were relatively broadened, indicating a decrease in the crystallite size, according to the Scherrer's formula.

The mechanical milling was followed by a sintering process. The optimal sintering temperature of 900 °C was optimized by measuring relative densities of $Al_{0.3}CoCrFeMnNi$ (>99%, indicating that a full densification) and by performing a post hardness test and grain-size measurements in the previous study[16]. After sintering, the XRD peaks exhibited a high intensity and were narrower, compared with those before the sintering, as shown in Fig. 1(b). Both $Al_{0.3}CoCrFeMnNi$ (without Y_2O_3) and $Al_{0.3}CoCrFeMnNi + 3\% Y_2O_3$ exhibited a combination of *fcc* (major phase) and B2 peaks (minor phase). The B2 crystal structure is often adopted by AB-type compounds and has been reported in many Al containing HEAs[1,11,16]. It has been previously reported that the volume fraction of the B2 phase in $Al_{0.3}CoCrFeMnNi$ is approximately 6 vol%[16]. The B2 phase has a space group of Pm3m, which is a primitive cubic structure. The chemical ordering within the B2 phase is based on the ordering of a body-centered cubic structure with different atomic species occupying the corners of the cube versus the body center of the cube. B2 alloys often exist over a range of compositions on either side of the stoichiometric composition. Deviations from the stoichiometric composition are accommodated by constitutional defects, i.e. either by vacancies on the deficient element's sublattice sites or by antisite atoms of the excess element[17]. In some compounds, e.g. aluminum-rich NiAl, the vacancies may be ordered[18]. The mechanical properties of B2 can be profoundly influenced by the composition of the intermetallic phase[17] and hence this phase in compositionally complex alloys like HEAs can be tuned over a wide range of compositions for tuning the mechanical properties.

Microstructural characterization of the constituent phases.
Detailed microstructural studies of the $Al_{0.3}CoCrFeMnNi$ (without Y_2O_3) sample showed the presence of *fcc*, B2, and chromium carbide phases[16]. Carbon measurements throughout the process showed that the alloy absorbed ~0.25 at% C after the mechanical milling, which reached the value of 0.4 at% C after the sintering in graphite dies; metal-carbides are often observed in SPS-processed alloys[16,19,20]. A scanning TEM (STEM) image of $Al_{0.3}CoCrFeMnNi$ (without Y_2O_3) is shown in Fig. 2(a), which shows the fully recrystallized microstructure consisting of nanograins. Some of the grains exhibit a darker contrast in Fig. 2a. This darker contrast can be attributed to carbides (Cr and C rich), and the B2 particles (Al, Mn and Ni rich) which are composed of relatively lighter elements and consequently appear darker in contrast in HAADF STEM images. However, some of the fcc grains may also appear dark due to diffraction contrast effects and strain differences.

The STEM image and selected area diffraction patterns (SADPs) of the phases observed in $Al_{0.3}CoCrFeMnNi + 3\% Y_2O_3$ are shown in Fig. 2(b) (and insets). The inset in the top-left part shows an SADP

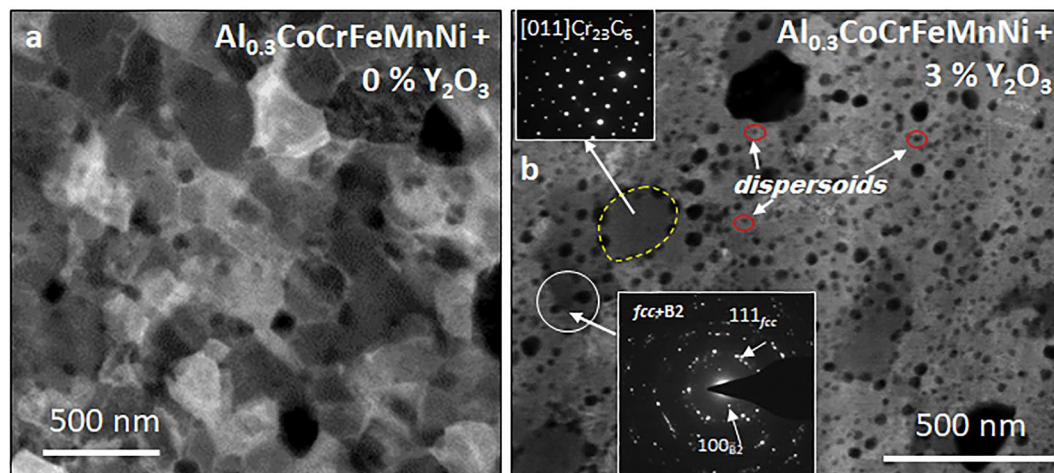**Figure 2.** Transmission Electron Microscopy: (**a**) STEM image from $Al_{0.3}CoCrFeMnNi + 0\%$ Y_2O_3 showing the nano-grains formed by the SPS process. (**b**) STEM image from $Al_{0.3}CoCrFeMnNi + 3\%$ Y_2O_3 shows the nano-grains along with the dark contrast dispersoids. Inset on top shows the SADP from Cr-carbide, and that on the bottom shows SADP from $fcc + B2$ phases.

of the $M_{23}C_6$ carbide phase along the [011] zone axis (outlined by the dotted yellow shape). The inset in the bottom-middle part shows an SADP of the fcc nanograins and B2 particles. These phases are formed during the sintering and do not contain Y_2O_3, as reported in our previous study[16]. Apart from the major sintered phase, small dark-contrast spherical features dispersed in the microstructure of $Al_{0.3}CoCrFeMnNi + 3\%$ Y_2O_3 were observed. These features were absent in the alloy without Y_2O_3, suggesting that they may be the dispersoids formed upon the addition of 3% Y_2O_3. However, it was challenging to precisely characterize the dispersoids using TEM; APT was employed for this purpose.

Compositional studies using APT. APT results for the 0%-Y_2O_3 and 3%-Y_2O_3 alloys are shown in Figs 3 and 4. Raw ion maps (Al (red), Cr (light green), Mn (magenta), Co (dark green), and Ni (blue)) from the fcc "matrix region" of the 0%-Y_2O_3 sample are shown in Fig. 3. The performed reconstruction reveals very homogeneous distributions of each of the chemical elements.

Ion maps of the 3%-Y_2O_3 alloy are shown in Fig. 4. Apart from the fcc matrix, the reconstruction reveals various microstructural features. In contrast to the 0%-Y_2O_3 sample, the fcc matrix in the 3%-Y_2O_3 alloy consists of fine-scale inhomogeneities, which are the distributed dispersoids, observed in the Al, Y, and O ion maps. Larger Al–Ni–Mn-rich particles are B2 precipitates formed in the alloy. In addition, a chromium–carbon-rich region is observed in the top-left part of the APT tip, which is the Cr-rich carbide ($M_{23}C_6$) formed during the SPS processing of the powders. Increases of the Al, Y, and O intensities within these regions can be clearly observed by visual inspection; the exact compositions of these phases are provided in Table 1. It is worth noting that Y_2O_3 can react with Al, forming a Y–Al–O complex oxide, *in-situ*, during the sintering of the powders. Amongst the possible oxides, yttria alumina monoclinic, yttria alumina perovskite, and yttria alumina garnet, have been reported[21,22]. However, the high contents of the other elements, Co, Cr, Fe, Mn, and Ni, suggest that owing to the high entropy state of the system, a Y–Al–Mn–Ni–Cr–Co–O complex oxide is formed through a surface reaction with the matrix[23–25].

In addition, studies on ODS of Al- and Ti-containing alloys demonstrated the formation of similar non-stoichiometric sub-oxide nanoprecipitates[25–27]. Ceri *et al.*[25] and Lindau *et al.*[27] suggested that, after MA, Y_2O_3 might not dissolve completely, and that the cores of the nanofeatures observed after sintering can consist of undissolved Y_2O_3. The cores can act as nuclei for other elements to segregate at the interface, which lowers the interface energy. London *et al.* showed that Cr could form a shell around oxide particles, leading to particles with a very small size and increased number density[28]. The composition of the oxide particles was determined to be ~9% Al, 12% Co, 9% Cr, 13% Cr, 16% Fe, 20% Ni, 10% Y and 10% O (all in at%). The high compositional complexity suggests substantially higher configurational entropy as compared to conventional Y_2O_3 particles in solute lean alloys. The development of entropically stabilized oxides (or high entropy oxides) has been an active area of interest in recent times[29–34]. Rost *et al.*[29] published on the existence of a new class of entropy stabilized mixed oxides with high configurational entropy. The authors of[29] also presented a hypothesis suggesting that entropy stabilization is particularly effective in a compound with ionic character. Lei *et al.*[30] developed ultrastable metal oxide nanotube arrays consisting of multiple oxide constituents by anodic oxidation of high-entropy alloy precursors. This has implications in the field of catalysis and energy storage.

The volume fraction of dispersoids (determined by APT) in the 3 vol.%Y_2O_3 reinforced alloy was determined to be 0.033. The radius of dispersoid particles was also determined from the APT analysis using iso-concentration surfaces to encapsulate the Al-rich dispersoids. The average radius of dispersoids was 0.95 nm in case of the 3 vol.% Y_2O_3 reinforced alloy. Further studies are ongoing to investigate the effect of the Y_2O_3 content on the composition and size of the complex oxide dispersoids formed in the alloy.
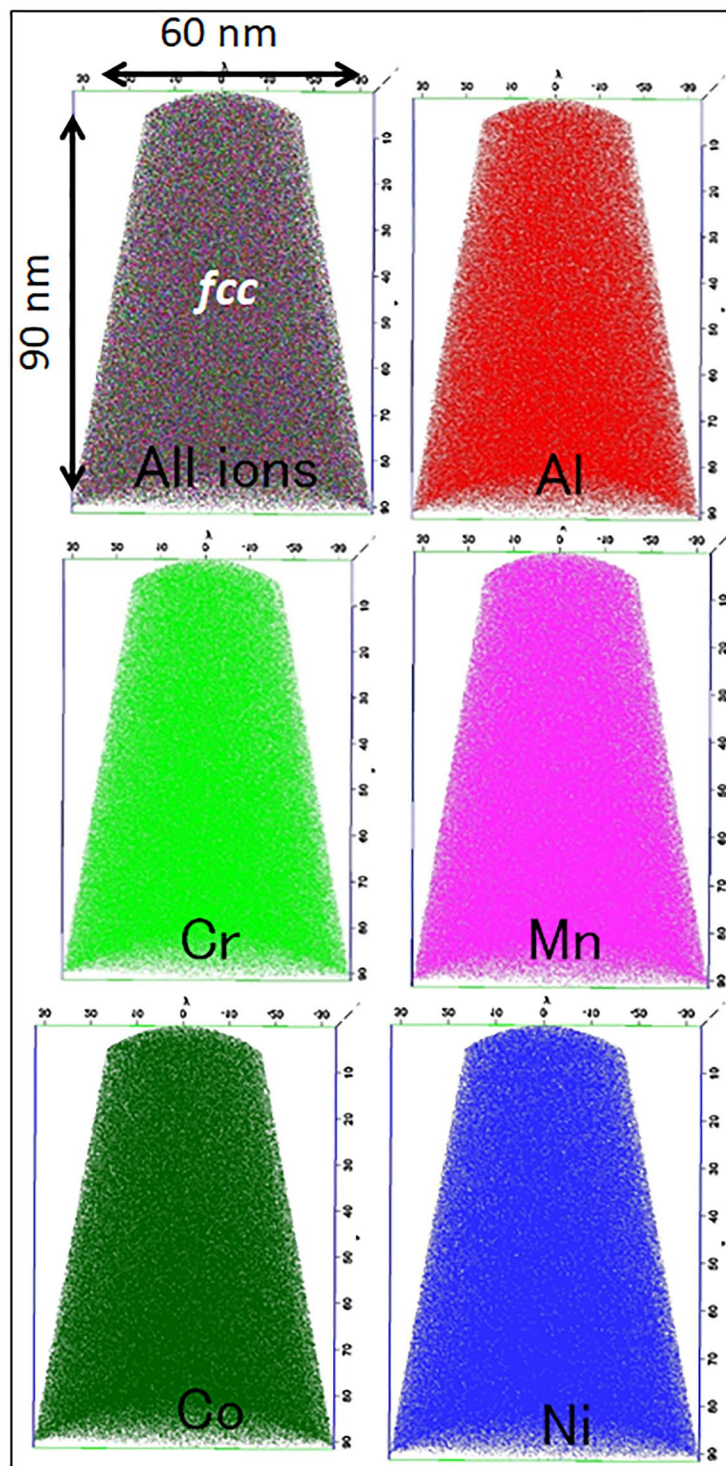
Figure 3. Atom Probe Tomography: 3-D reconstruction of APT data from $Al_{0.3}CoCrFeMnNi + 0\%$ Y_2O_3 showing a homogeneous distribution of all elements.

Compressive stress–strain curves for the $Al_{0.3}CoCrFeMnNi$ alloys without Y_2O_3 and with 3% Y_2O_3 at ambient temperature are shown in Fig. 5. At 0% Y_2O_3, $Al_{0.3}CoCrFeMnNi$ exhibits a yield strength of 979 MPa with a strain of 39.3%; at 3% Y_2O_3, the yield strength increased to 1,759 MPa (an increase of ~80%), while the strain decreased to 19.8%. This indicates that the Y_2O_3 dispersoids act as a barrier to dislocation motion, enhancing the mechanical properties, still maintaining a reasonable amount of ductility.

Considering the sample processing parameters and apparatus used for processing the base alloy (0% Y_2O_3) and the 3% Y_2O_3 reinforced alloy were same, the Hall-Petch strengthening due to grain size effect, composite strengthening due to intermetallic B2 and carbide particles and solid solution strengthening can be assumed
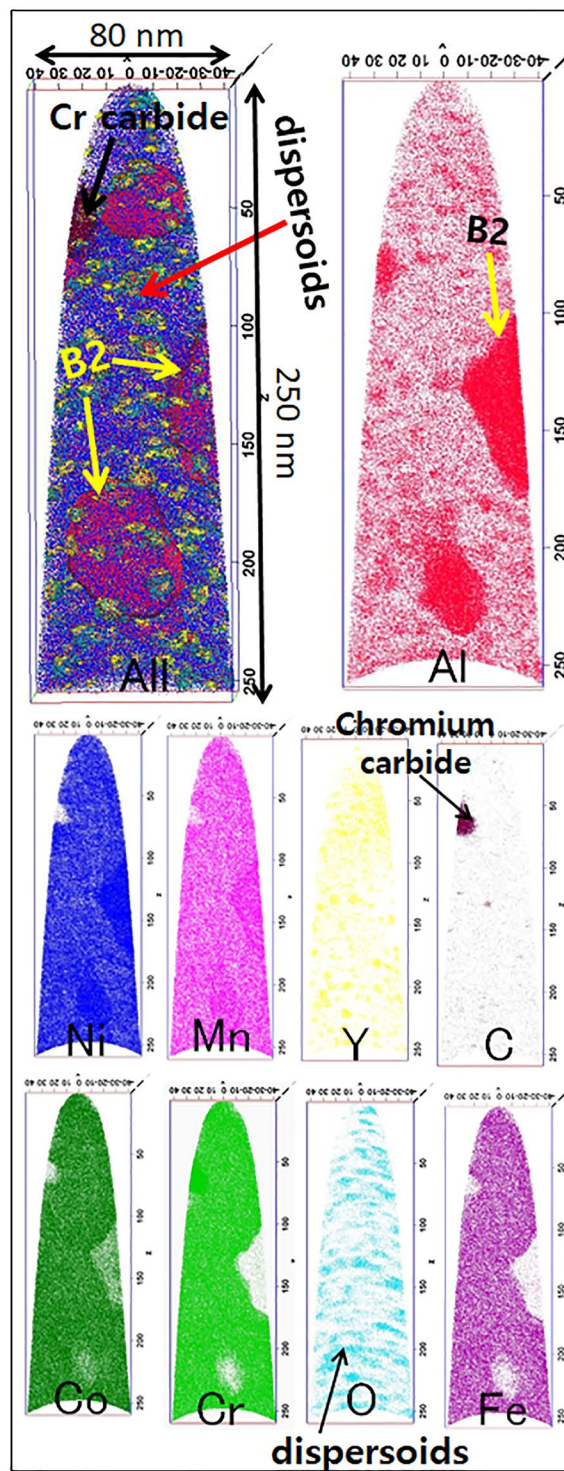
Figure 4. Atom Probe Tomography: 3-D reconstruction of APT data from $Al_{0.3}CoCrFeMnNi + 3\%\ Y_2O_3$ showing the presence of various features as labeled in the figure. Top left reconstruction shows an all-ions map followed by the reconstructions showing individual ion maps for various elements. Fine scale inhomogeneity within the matrix clearly seen in Al, Y and O maps correspond to the dispersoids.

similar in both alloys. Hence, the yield strength of the base, which is ~980 MPa if assumed to be due to the grain size and solid solution strengthening, the strength increment on reinforcing the alloy with 3% Y_2O_3 can be estimated to be ~780 MPa. Theoretically, the dispersion strengthening can be modeled using the dispersed-barrier hardening model[35]. This model is based on the intersection of the obstacles with the dislocation glide plane[36] using geometrical estimations:

Phase	Compositions [at%]								
	Al	Co	Cr	Fe	Mn	Ni	Y	C	O
fcc	5.7 ± 0.09	18.3 ± 0.03	15.7 ± 0.05	19.3 ± 0.4	18.4 ± 0.03	21.2 ± 0.08	1.04 ± 0.02	0.1 ± 0.1	1.01 ± 0.02
B2	19.8 ± 0.04	10 ± 0.03	0.7 ± 0.1	3.9 ± 0.04	24.9 ± 0.01	38.2 ± 0.01	2.3 ± 0.07	0	1.9 ± 0.1
Cr-carbide	0	4.5 ± 0.09	59.3 ± 0.09	9.8 ± 0.08	8.8 ± 0.03	4.3 ± 0.05	0	12.7 ± 0.02	0
Dispersoid	8.7 ± 0.07	12.1 ± 0.04	9.2 ± 0.05	13 ± 0.07	16.1 ± 0.04	20.3 ± 0.03	9.9 ± 0.04	0	9.7 ± 0.03

Table 1. Compositions of various phases by atom probe tomography of $Al_{0.3}CoCrFeMnNi + 3\%$ Y_2O_3.

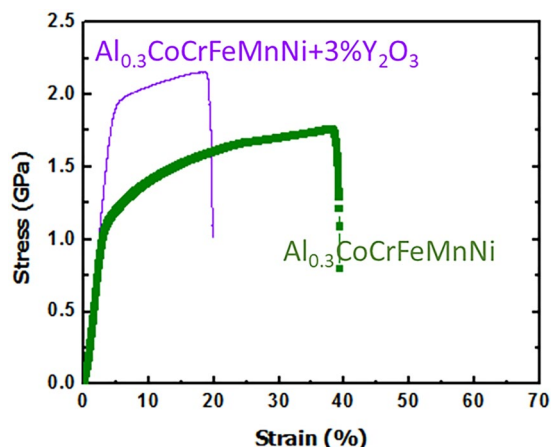**Figure 5.** Performance under mechanical loading. (**a**) Compressive stress-strain curves of $Al_{0.3}CoCrFeMnNi$ 0% Y_2O_3 and ODS $Al_{0.3}CoCrFeMnNi$ with 3% Y_2O_3.

$$\Delta\sigma = 0.8\,M\alpha\,(r)Gb/\lambda \tag{1}$$

where $\alpha(r)$ is the obstacle strength-coefficient and it represents the strength of the obstacles to impede dislocation motion. Alinger[37] proposed a function of $\alpha(r)$,

$$\alpha(r) = -0.017 + 0.374 \log\left(\frac{r}{2b}\right) \tag{2}$$

in case of an impenetrable obstacle, $\alpha(r) = 1$ and Orowan by-pass mechanism can be used. In the current work, $\alpha(r)$ is ~0.08 where a range of $\alpha(r)$ values approximately lying between 0.05 and 0.30 clearly indicates that the fine scale nanodispersoids are relatively soft obstacles, and can be sheared by dislocations[38].

G, b (0.255 nm for CoCrFeNiMn)[39], f and r denote the shear modulus, the Burgers vector and the dispersoid size, respectively. λ is the average planar center-to-center distance between nano-dispersoids and is given by:

$$\lambda = 2\sqrt{\frac{2}{3}}\,r\left(\sqrt{\frac{\pi}{4f}} - 1\right) \tag{3}$$

In current work it is noted that the direct-strengthening calculated from the dispersed-barrier hardening model is about one-third of the Orowan by-pass model. Siska *et al.* in their assessment of strengthening mechanisms arising from different oxide particles in 9Cr ODS steel showed that the dispersed-barrier hardening model works better for Y_2O_3 dispersoids[40].

The average radius of dispersoids was 0.95 nm in case of the 3 vol.% Y_2O_3 reinforced alloy. This APT data reveals dispersion strengthening (σ, according to Eq. (1)) in 3 vol.% Y_2O_3 reinforced $Al_{0.3}CoCrFeMnNi$ alloy was ~695 MPa in good agreement with the experimentally estimated strength estimate of ~780 MPa. This establishes that the dispersion strengthening mechanism plays an important role in imparting high compressive strength in such ODS HEAs. The difference in the experimental value and the calculation could be explained based on the non-additive nature of the various mechanisms. The strengthening contributions due to Hall-Petch, solid solution strengthening and dispersion strengthening can influence each other and the dislocation density of the matrix. This will also change the dislocation strengthening of the base matrix.

Furthermore, a comparison with other *fcc*-based HEAs[41–49] is summarized in Fig. 6 where the compressive YS vs fracture strain is presented. The analyzed 3%-Y_2O_3 HEA is located in the upper-right part of the diagram, which indicates that it outperforms most of the reported HEAs. It seems that the current alloy has the most desirable combination of strength and ductility among *fcc*-based HEAs materials. For a study of the detailed deformation mechanisms of dispersion-strengthened HEAs, tensile tests, creep and fatigue tests should be conducted in the future.
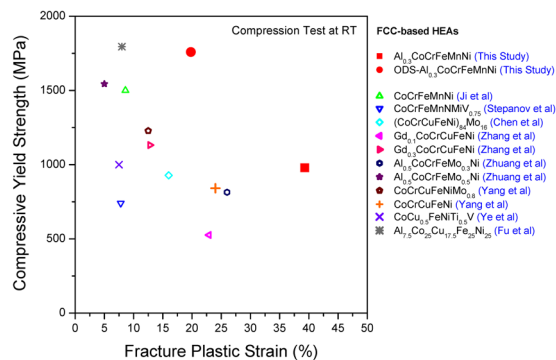
Figure 6. The plot of compressive yield strength-fracture strain combinations from various fcc-containing high strength HEAs including the current alloys, showing great advantage of the current HEAs.

Conclusion

In this study, $Al_{0.3}CoCrFeMnNi + 3$ vol.% Y_2O_3 HEAs were prepared by planetary ball milling for 36 h followed by spark plasma sintering at 900 °C under a pressure of 50 MPa for 10 min. The SPS yielded a nano-grained microstructure consisting of *fcc*, B2, and $M_{23}C_6$ carbide phases. Along with these phases, the alloy exhibited an even finer-scale complex-oxide dispersed phase, formed through an *in-situ* reaction during the sintering, whose morphology was investigated using APT. The dispersoids led to an increase in the yield strength and a decrease in ductility. The large increase in the yield strength could be attributed to the dispersion strengthening, indicating the effectiveness of the employed strengthening method. This study presented a novel methodology for the formation of complex oxide dispersoids in compositionally complex HEAs, which can also be applied to other alloys.

Methods

High-purity powders of Al, Co, Mn, Ni (particle size <15 μm), Cr (particle size <45 μm) (Kojundo Co, Ltd.), Fe (particle size <25 μm), and Y_2O_3 (particle size <10 μm) (Sigma Aldrich) were used to prepare $Al_{0.3}CoCrFeMnNi$ (expressed in molar ratio) with 3 vol.% Y_2O_3 by planetary ball milling for 36 h. Stainless-steel vials and stainless-steel balls with a diameter of 1.1 cm were employed, using a ball-to-powder mass ratio of 15:1 in an argon atmosphere including n-heptane as a process control agent (PCA) to reduce the cold welding of the powder. The as-milled powders were then consolidated using spark plasma sintering (Dr. Sinter Lab. SPS-515S) at 900 °C in a vacuum atmosphere (1.5×10^{-5} Bar) for 10 min under a uniaxial pressure of 50 MPa, at a heating rate of 100 °C/min.

The crystal structures of the milled powders and sintered alloys were investigated using an X-ray diffractometer (XRD, Rigaku D/Max-2500) with Cu-K_α radiation. Their microstructures were observed using transmission electron microscopy (TEM) (Tecnai G2 F30 S-Twin) and APT (Cameca 3000X HR local electrode atom probe (LEAP)). Thin TEM lamellae and tapered APT needles were produced from site-specific regions of interest, for TEM and APT analyses, respectively. The lamellae were prepared by focused ion beam (FIB) milling using an FEI Nova 200 NanoLab Dual Beam system equipped with a Ga+ ion source and Pt gas injection system. The densities of the sintered alloys were measured using the Archimedes' principle. The compressive properties of the specimens (cylindrical shape, with a diameter of 3 mm and height of 6 mm) were investigated using an INSTRON 5583 system at a crosshead speed of 0.2 mm/min.

Impact Statement.   An unprecedented yield strength of $Al_{0.3}CoCrFeMnNi$ up to 1759 MPa was achieved by the *in-situ* formation of the compositionally complex nanoscale dispersoids in the high entropy alloy.

Data Availability Statement

The data that support the findings of this study are available within the paper. Any further information or clarification is available from the corresponding author upon reasonable request.

References

1. Yeh, J. W. *et al.* Nanostructured high-entropy alloys with multiple principal elements: Novel alloy design concepts and outcomes. *Adv. Eng. Mater.* **6**(5), 299–303 (2004).
2. Stepanov, N. *et al.* Effect of cryo-deformation on structure and properties of CoCrFeNiMn high-entropy alloy. *Intermetallics.* **59**, 8–17 (2015).
3. Schuh, B. *et al.* Mechanical properties, microstructure and thermal stability of a nanocrystalline CoCrFeMnNi high-entropy alloy after severe plastic deformation. *Acta Materialia.* **96**, 258–268 (2015).
4. Cantor, B., Chang, I. T. H., Knight, P. & Vincent, A. J. B. Microstructural development in equiatomic multicomponent alloys. *Materials Science and Engineering: A.* **375**, 213–218 (2004).
5. Yao, M. J., Pradeep, K. G., Tasan, C. C. & Raabe, D. A novel, single phase, non-equiatomic FeMnNiCoCr high-entropy alloy with exceptional phase stability and tensile ductility. *Scripta Materialia.* **72**, 5–8 (2014).
6. Otto, F. *et al.* The influences of temperature and microstructure on the tensile properties of a CoCrFeMnNi high-entropy alloy. *Acta Materialia.* **61**(15), 5743–5755 (2013).
7. Laplanche, G., Horst, O., Otto, F., Eggeler, G. & George, E. P. Microstructural evolution of a CoCrFeMnNi high-entropy alloy after swaging and annealing. *Journal of Alloys and Compounds.* **647**, 548–557 (2015).
8. Liu, W. H., Wu, Y., He, J. Y., Nieh, T. G. & Lu, Z. P. Grain growth and the Hall–Petch relationship in a high-entropy FeCrNiCoMn alloy. *Scripta Materialia.* **68**(7), 526–529 (2013).

9. He, J. Y. *et al*. Effects of Al addition on structural evolution and tensile properties of the FeCoNiCrMn high-entropy alloy system. *Acta Materialia*. **62**, 105–113 (2014).

10. Gwalani, B. *et al*. (2017). Optimizing the coupled effects of Hall-Petch and precipitation strengthening in a Al0. 3CoCrFeNi high entropy alloy. *Materials & Design*. **121**, 254–260 (2014).

11. Gwalani, B. *et al*. Stability of ordered L12 and B2 precipitates in face centered cubic based high entropy alloys-Al0. 3CoFeCrNi and Al0. 3CuFeCrNi2. *Scripta Materialia*. **123**, 130–134 (2016).

12. Humphry-Baker, S. A. & Schuh, C. A. Suppression of grain growth in nanocrystalline Bi2Te3 through oxide particle dispersions. *Journal of Applied Physics*. **116**(17), 173505 (2014).

13. Kaminskii, A. A. *et al*. Microhardness and fracture toughness of Y2O3-and Y3Al5O12-based nanocrystalline laser ceramics. *Crystallography Reports*. **50**(5), 869–873 (2005).

14. Hadraba, H. *et al*. Oxide dispersion strengthened CoCrFeNiMn high-entropy alloy. *Materials Science and Engineering: A*. **689**, 252–256 (2017).

15. Gwalani, B. *et al*. Cu assisted stabilization and nucleation of L1 2 precipitates in Al 0.3 CuFeCrNi 2 fcc-based high entropy alloy. *Acta Materialia*. **129**, 170–182 (2017).

16. Pohan, R. M. *et al*. Microstructures and mechanical properties of mechanically alloyed and spark plasma sintered Al0. 3CoCrFeMnNi high entropy alloy. *Materials Chemistry and Physics*. **210**, 62–70 (2018).

17. Baker, I. A review of the mechanical properties of B2 compounds. *Materials Science and Engineering: A*. **192**, 1–13 (1995).

18. Noebe, R. D., Bowman, R. R. & Nathal, M. V. Physical and mechanical properties of the B2 compound NiAl. *International Materials Reviews*. **38**(4), 193–232 (1993).

19. Praveen, S., Anupam, A., Sirasani, T., Murty, B. S. & Kottada, R. S. Characterization of oxide dispersed AlCoCrFe high entropy alloy synthesized by mechanical alloying and spark plasma sintering. *Transactions of the Indian Institute of Metals* **66**(4), 369–373 (2013).

20. Sriharitha, R., Murty, B. S. & Kottada, R. S. Alloying, thermal stability and strengthening in spark plasma sintered AlxCoCrCuFeNi high entropy alloys. *Journal of Alloys and Compounds*. **583**, 419–426 (2014).

21. Phaniraj, M. P., Kim, D. I., Shim, J. H. & Cho, Y. W. Microstructure development in mechanically alloyed yttria dispersed austenitic steels. *Acta materialia*. **57**(6), 1856–1864 (2009).

22. Guo, X. & Sakurai, K. Formation of yttrium aluminum perovskite and yttrium aluminum garnet by mechanical solid-state reaction. *Japanese Journal of Applied Physics*. **39**(3R), 1230 (2000).

23. Yu, H., Ukai, S., Hayashi, S. & Oono, N. H. Effect of Cr and Y2O3 on the oxidation behavior of Co-based oxide dispersion strengthened superalloys at 900 °C. *Corrosion Science*. **127**, 147–156 (2017).

24. Zhang, L., Ukai, S., Hoshino, T., Hayashi, S. & Qu, X. Y2O3 evolution and dispersion refinement in Co-base ODS alloys. *Acta Materialia*. **57**(12), 3671–3682 (2009).

25. Williams, C. A., Marquis, E. A., Cerezo, A. & Smith, G. D. Nanoscale characterisation of ODS–Eurofer 97 steel: an atom-probe tomography study. *Journal of Nuclear Materials*. **400**(1), 37–45 (2010).

26. Alinger, M. J. *et al*. Positron annihilation characterization of nanostructured ferritic alloys. *Materials Science and Engineering. A*. **518**(1-2), 150–157 (2009).

27. Lindau, R., Möslang, A., Schirra, M., Schlossmacher, P. & Klimenkov, M. Mechanical and microstructural properties of a hipped RAFM ODS-steel. *Journal of Nuclear Materials*. **307**, 769–772 (2002).

28. London, A. J. *et al*. Comparison of atom probe tomography and transmission electron microscopy analysis of oxide dispersion strengthened steels. *In Journal of Physics: Conference Series*. **522**, 012028 (2014).

29. Rost, C. M. *et al*. Entropy-stabilized oxides. *Nature communications* **6**, 8485 (2015).

30. Lei, Z. *et al*. Ultrastable metal oxide nanotube arrays achieved by entropy-stabilization engineering. *Scripta Materialia* **146**, 340–343 (2018).

31. Chen, H. *et al*. Entropy-stabilized metal oxide solid solutions as CO oxidation catalysts with high-temperature stability. *Journal of Materials Chemistry A* **6**(24), 11129–11133 (2018).

32. Anand, G., Wynn, A. P., Handley, C. M. & Freeman, C. L. Phase stability and distortion in high-entropy oxides. *Acta Materialia* **146**, 119–125 (2018).

33. Chen, K. *et al*. A five-component entropy- stabilized fluorite oxide. *Journal of the European Ceramic Society* **38**(11), 4161–4164 (2018).

34. Biesuz, M., Spiridigliozzi, L., Dell'Agli, G., Bortolotti, M. & Sglavo, V. M. Synthesis and sintering of (Mg, Co, Ni, Cu, Zn) O entropy-stabilized oxides obtained by wet chemical methods. *Journal of Materials Science* **53**(11), 8074–8085 (2018).

35. Kim, J. H. *et al*. Temperature dependence of strengthening mechanisms in the nanostructured ferritic alloy 14YWT: Part II—Mechanistic models and predictions. *Materials Science & Engineering A* **559**, 111–118 (2013).

36. Zinkle, S. J. & Matsukawa, Y. Observation and analysis of defect cluster production and interactions with dislocations. *Journal of nuclear materials* **329**, 88–96 (2004).

37. Alinger, M. J., Odette, G. R. & Hoelzer, D. T. On the role of alloy composition and processing parameters in nanocluster formation and dispersion strengthening in nanostuctured ferritic alloys. *Acta Materialia* **57**(2), 392–406 (2009).

38. Odette, G. R., Alinger, M. J. & Wirth, B. D. Recent developments in irradiation-resistant steels. *Annu. Rev. Mater. Res*. **38**, 471–503 (2008).

39. He, J. Y. *et al*. Steady state flow of the FeCoNiCrMn high entropy alloy at elevated temperatures. *Intermetallics*. **55**, 9–14 (2014).

40. Siska, F. *et al*. Strengthening mechanisms of different oxide particles in 9Cr ODS steel at high temperatures. *Materials Science and Engineering: A* (2018).

41. Miracle, D. B. & Senkov, O. N. A critical review of high entropy alloys and related concepts. *Acta Materialia*. **122**, 448–511 (2017).

42. Ye, Y. F., Wang, Q., Lu, J., Liu, C. T. & Yang, Y. High-entropy alloy: challenges and prospects. *Materials Today*. **19**(6), 349–362 (2016).

43. Ji, W. *et al*. Alloying behavior and novel properties of CoCrFeNiMn high-entropy alloy fabricated by mechanical alloying and spark plasma sintering. *Intermetallics* **56**, 24–27 (2015).

44. Stepanov, N. D. *et al*. Effect of V content on microstructure and mechanical properties of the CoCrFeMnNiVx high entropy alloys. *Journal of Alloys and Compounds* **628**, 170–185 (2015).

45. Chen, R. *et al*. Composition design of high entropy alloys using the valence electron concentration to balance strength and ductility. *Acta Materialia* **144**, 129–137 (2018).

46. Zhang, L. J. *et al*. Microstructure and mechanical behaviors of GdxCoCrCuFeNi high-entropy alloys. *Materials Science and Engineering: A* **707**, 708–716 (2017).

47. Yang, Q. *et al*. Microstructures and properties of CoCrCuFeNiMox high-entropy alloys fabricated by mechanical alloying and spark plasma sintering. *Powder Metallurgy* **61**(2), 115–122 (2018).

48. Ye, H., Zhan, Y. & Nie, N. Development of novel CoCu0. 5FeNiVTi x (x = 0, 0.5, 1, 1.5, 2) high-entropy alloys. *Materials Science and Technology* **34**(8), 952–960 (2018).

49. Fu, Z. *et al*. Microstructure and strengthening mechanisms in an FCC structured single-phase nanocrystalline Co25Ni25Fe25Al7. 5Cu17. 5 high-entropy alloy. *Acta Materialia* **107**, 59–71 (2016).

Acknowledgements

Author Contributions

B. Gwalani, R.M. Pohan, J. Lee, B. Lee participated in the experiments. R. Banerjee, H.J. Ryu, S.H. Hong analyzed the results. All authors contributed to the manuscript preparation and reviewed the manuscript.

Additional Information

Competing Interests: The authors declare no competing interests.

Publisher's note: Springer Nature remains neutral with regard to jurisdictional claims in published maps and institutional affiliations.